



UNIVERSITÀ  
DI TRENTO

# Modelling the impact of aortic aneurysm prostheses on systemic haemodynamics

Report of the Computational Haemodynamics course project

By

Stefano Costa

Lecturer

Prof. Lucas Omar Müller

# Contents

<b>1</b>	<b>Introduction</b>	<b>3</b>
<b>2</b>	<b>Methods</b>	<b>3</b>
2.1	Mathematical models . . . . .	3
2.1.1	Blood flow equations . . . . .	3
2.1.2	Quasi-linear form . . . . .	4
2.1.3	Riemann problem . . . . .	4
2.2	Numerical Methods . . . . .	6
2.2.1	Space and time discretization . . . . .	6
2.2.2	First order scheme . . . . .	6
2.2.3	HLL numerical flux (Harten et al. 1983) . . . . .	6
2.2.4	MUSCL-Hancock (MH) scheme (Leer 1979) . . . . .	7
2.3	Boundary conditions . . . . .	7
2.3.1	Inflow boundary conditions . . . . .	7
2.3.2	Terminal boundary conditions . . . . .	8
2.3.3	Junction coupling conditions . . . . .	8
2.4	Empirical convergence rate . . . . .	8
2.5	Assessment of computational errors . . . . .	9
2.6	Modeling of endoleak and endograft . . . . .	9
<b>3</b>	<b>Results</b>	<b>10</b>
3.1	Task 1 - Empirical convergence rates . . . . .	10
3.2	Task 2 - Modelling blood flow in the arterial network used in (Xiao et al. 2014) . . . . .	11
3.3	Task 3 - Impact of aortic aneurysm endografts on systemic haemodynamics . . . . .	13
<b>4</b>	<b>Discussion</b>	<b>17</b>
4.1	Task 1 - Empirical convergence rates . . . . .	17
4.2	Task 2 - Modelling blood flow in the arterial network used in (Xiao et al. 2014) . . . . .	17
4.3	Task 3 - Impact of aortic aneurysm endografts on systemic haemodynamics . . . . .	17
4.3.1	Stent case . . . . .	17
4.3.2	Endoleak case . . . . .	18
<b>5</b>	<b>Conclusions</b>	<b>18</b>

## Abstract

Recent decades have witnessed significant advancements in modeling and simulation techniques aimed at unraveling the complexities of cardiovascular diseases, which remain a predominant cause of global morbidity and mortality. Comparative analysis between one-dimensional (1D) and three-dimensional (3D) cardiovascular models is a practiced approach in the scientific community, with each model offering distinct advantages and specific trade-offs. Despite the computational gap, studies indicate that 1D models can produce comparable results to 3D models under specific conditions. In this report we study a 1D model by analyzing its results in several ways. Initially, we examine the empirical convergence rates of the numerical methods employed, ensuring the correctness of the implementation. Then, we replicate what was obtained in (Xiao et al. 2014) so that the results can be compared. Finally, we use the model to simulate a thoracic endograft and endoleak, assessing whether the results produced, in terms of pressures and flows, are in line with the scientific literature.

## 1 Introduction

Cardiovascular disease remains a leading cause of morbidity and mortality worldwide (Roth et al. 2020; Townsend et al. 2016), necessitating continuous advancements in modeling and simulation techniques to enhance our understanding of its intricacies (Morris et al. 2015). The comparison between 1D and 3D models has proven to be a very useful tool within the realm of cardiovascular modeling (Bezerra et al. 2018).

One-dimensional (1D) and three-dimensional (3D) cardiovascular models represent two complementary approaches to simulate the complex dynamics of the cardiovascular system. While 1D models are renowned for their computational efficiency and ability to provide a global overview of cardiovascular hemodynamics (Gray et al. 2018), 3D models offer a more detailed and anatomically realistic representation of the vasculature (Taylor et al. 2009).

The choice between these modeling paradigms is often dictated by the research objectives and computational resources available. Notably, 3D models necessitate substantial computational resources due to their intricate spatial representation and detailed simulations. In contrast, 1D models, with their simplified geometry and lower-dimensional representations, require less computing power, making them a viable option for studies with limited resources. Despite the inherent computational disparities studies have suggested that 1D models can yield results comparable to their 3D counterparts under certain conditions (Xiao et al. 2014).

In this report is used a 1D model with the characteristics explained in [Section 2.1](#). The objective of the report is to investigate the extent to which the model used is able to replicate the 1D and 3D results of (Xiao et al. 2014) ([Section 3.2](#)). Next in [Section 3.3](#), the model is used in the simulation of a thoracic endograft and endoleak to check whether the results are in line with the scientific literature. Before that, however, in [Section 3.1](#) the empirical convergence rates of the numerical methods used are tested to make sure of the reliability of the implementation.

## 2 Methods

### 2.1 Mathematical models

#### 2.1.1 Blood flow equations

In the 1D formulation, the *blood flow equations* describe the dynamics of a single blood vessel. Each vessel is depicted as a deformable tube characterized by a single axial coordinate, denoted as  $x$ . Under the assumption of impermeable vessel walls and incompressible Newtonian fluid blood, the blood flow equations (BFEs), derived from conservation principles as in (Formaggia et al. 2009), are expressed as

$$\begin{cases} \partial_t A + \partial_x(Au) = 0 & \text{Mass conservation equation,} \\ \partial_t(Au) + \partial_x(\alpha Au^2) + \frac{A}{\rho} \partial_x P = -R_v u & \text{Momentum balance equation,} \end{cases} \quad (1)$$

where  $A(x, t)$ ,  $u(x, t)$ , and  $P(x, t)$  denote the *vessel cross-sectional area*, the *cross-sectional average velocity of blood*, and the *pressure* respectively, at position  $x$  and time  $t$ . The constant *density of blood* is represented by  $\rho$ , while  $\alpha$  represents the *momentum correction factor*, which we assumed to be 1. The term  $R_v$  denotes the *viscous resistance of the flow per unit length of the tube* and is defined as  $R_v = -\frac{\mu}{\rho} \int_{\partial S} \frac{\partial s}{\partial \vec{n}_{\partial S}} d\gamma$ , where  $\vec{n}_{\partial S}$  is the outer normal vector to the boundary of the vessel cross-section  $\partial S$ , and  $\mu$  is the constant *blood viscosity*. The velocity profile  $s$  is assumed to be known as

$$s(r) = \frac{\delta + 2}{\delta} \left( 1 - \left( \frac{r}{R} \right)^\delta \right), \quad (2)$$

where  $r \in [0, R]$  with  $R$  being the *vessel's radius*, and the choice of  $\delta$  changes the type of the velocity profile:  $\delta = 2$  leads to a parabolic profile, while  $\delta > 2$  leads to a blunted profile. Following the methodology described in (Xiao et al. 2014), in [Section 3.2](#) and [Section 3.3](#) the value  $\delta = 9$  is considered, that yields  $R_v = \frac{22\mu}{\rho}\pi$ .

With three unknowns ( $A(x, t)$ ,  $u(x, t)$ , and  $P(x, t)$ ) and only two equations in system (1), the inclusion of an additional equation, known as the *tube law*, is required. This equation establishes a relationship between pressure and vessel wall

displacement via the cross-sectional area  $A$ . In this report, a tube law of the following form has been adopted:

$$P(x, t) = P_e + P_0 + K\mathcal{E} = P_e + P_0 + \frac{4}{3} \frac{E h_0}{R_0} \left( \sqrt{\frac{A(x, t)}{A_0}} - 1 \right), \quad (3)$$

where  $P_e$  denotes the *external pressure*,  $R_0$  the reference radius (meaning that small deformations are assumed around  $R_0$ ),  $P_0$  the *reference pressure*,  $A_0 = \pi R_0^2$  the *reference area*,  $h$  the *vessel wall thickness* and  $h_0 = h(R_0)$ ,  $E$  the *Young's modulus*. In (3)  $K$  denotes the *stiffness coefficient* while  $\mathcal{E}$  denotes the *strain*, defined as

$$K = \frac{E h_0}{(1 - \nu^2) R_0}, \quad \mathcal{E} = \frac{R - R_0}{R_0} = \sqrt{\frac{A}{A_0}} - 1, \quad (4)$$

where  $\nu$  is the *Poisson ratio*, assumed to be equal to 0.5.

## 2.1.2 Quasi-linear form

System (1) can be written in conservation-law form as

$$\partial_t \mathbf{Q} + \partial_x \mathbf{F}(\mathbf{Q}) = \mathbf{S}(\mathbf{Q}), \quad (5)$$

where

$$\mathbf{Q} = \begin{bmatrix} A \\ Au \end{bmatrix} = \begin{bmatrix} A \\ Q \end{bmatrix}, \quad \mathbf{F}(\mathbf{Q}) = \begin{bmatrix} Au \\ Au^2 + \frac{\beta}{3\rho} A^{3/2} \end{bmatrix}, \quad \mathbf{S}(\mathbf{Q}) = \begin{bmatrix} 0 \\ -R_v u \end{bmatrix},$$

are called *state vector*, *physical flux vector*, and *physical source term vector* respectively, and  $\beta = \frac{K}{\sqrt{A_0}}$ . Equivalently, equation (5) can be written in a quasi-linear form as

$$\partial_t \mathbf{Q} + \mathbf{A}(\mathbf{Q}) \partial_x \mathbf{Q} = \mathbf{S}(\mathbf{Q}), \quad (6)$$

where  $\mathbf{A}(\mathbf{Q}) = \begin{bmatrix} 0 & 1 \\ c^2 - u^2 & 2u \end{bmatrix}$  is the *Jacobian matrix* and  $c^2 = \frac{\beta}{2\rho} \sqrt{A}$  is the *wave speed*. The eigenvalues of  $\mathbf{A}(\mathbf{Q})$  are  $\lambda_1 = u - c$ ,  $\lambda_2 = u + c$ . The right eigenvectors are  $\mathbf{R}_1 = \gamma_1 \begin{bmatrix} 1 \\ u - c \end{bmatrix}$  and  $\mathbf{R}_2 = \gamma_2 \begin{bmatrix} 1 \\ u + c \end{bmatrix}$ , corresponding respectively to  $\lambda_1$  and  $\lambda_2$ , where  $\gamma_i$  for  $i = 1, 2$  are arbitrary scaling factors. Choosing the scaling factors equal to 1, the matrix of right eigenvectors and its inverse can be written as

$$\mathbf{R}(\mathbf{Q}) = \begin{bmatrix} 1 & 1 \\ u - c & u + c \end{bmatrix}, \quad \mathbf{R}^{-1}(\mathbf{Q}) = \begin{bmatrix} \frac{c+u}{2c} & -\frac{1}{2c} \\ \frac{c-u}{2c} & \frac{1}{2c} \end{bmatrix}. \quad (7)$$

Under the assumptions  $u \in \mathbb{R}$  and  $A \in \mathbb{R}_{>0}$ , system (6) is strictly hyperbolic, since  $\lambda_1, \lambda_2 \in \mathbb{R}$  and  $\lambda_1 \neq \lambda_2$ . Moreover, it can be shown that the  $\lambda_1$ - and  $\lambda_2$ -characteristic fields are *genuinely non-linear*. Considering a tube law of the form (3), the generalised Riemann invariants for the  $\lambda_1$ - and  $\lambda_2$ -characteristic fields are respectively

$$\Gamma_1 = u + \int \frac{c(A)}{A} dA = u + 4c = \text{constant} \quad \text{and} \quad \Gamma_2 = u - \int \frac{c(A)}{A} dA = u - 4c = \text{constant}.$$

## 2.1.3 Riemann problem

Consider the following Riemann problem for the BFEs

$$\begin{aligned} \partial_t \mathbf{Q} + \mathbf{A}(\mathbf{Q}) \partial_x \mathbf{Q} &= \mathbf{S}(\mathbf{Q}) \quad x \in \mathbb{R}, t > 0, \\ \mathbf{Q}(x, 0) &= \begin{cases} \mathbf{Q}_L, & \text{if } x < x_{gate} \\ \mathbf{Q}_R, & \text{if } x > x_{gate} \end{cases}. \end{aligned} \quad (8)$$

Without loss of generality, we considered  $x_{gate} = 0$ . Firstly, it is necessary to determine the state  $\mathbf{Q}_* = [A_*, A_* u_*]^T$  that connects  $\mathbf{Q}_L$  and  $\mathbf{Q}_R$  via wave relations. Finding  $A_*$  requires solving the nonlinear equation

$$f_R(A_*; A_R) + f_L(A_*; A_L) + u_R - u_L = 0,$$

where

$$f_K(A_*; A_K) = \begin{cases} \frac{4(c_* - c_K)}{\left( \frac{d(A_* - A_K)(A_*^{3/2} - A_K^{3/2})}{A_K A_*} \right)^{1/2}} & \text{if } A_* \leq A_K \quad (\text{Rarefaction}) \\ \left( \frac{d(A_* - A_K)(A_*^{3/2} - A_K^{3/2})}{A_K A_*} \right)^{1/2} & \text{if } A_* > A_K \quad (\text{Shock}) \end{cases} \quad K \in \{L, R\}, \quad (9)$$

where  $d = \frac{\beta}{3\rho}$ . Equation (9) can be solved numerically, for example by using Newton's method. Once  $A_*$  is available,  $u_*$  is computed as

$$u_* = \frac{1}{2}(u_R + u_L) + \frac{1}{2}(f_R(A_*; A_R) - f_L(A_*; A_L)). \quad (10)$$

Furthermore, in the case of shock waves we need to compute shock speeds as

$$S_L = u_L - \frac{M_L}{A_L}, \quad S_R = u_R + \frac{M_R}{A_R}, \quad (11)$$

where

$$M_K = \left( \frac{dA_* A_K (A_*^{3/2} - A_K^{3/2})}{A_* - A_K} \right)^{1/2}, \quad K \in \{L, R\}. \quad (12)$$

After obtaining  $u_*$  we can sample using primitive variables  $\mathbf{W} = [A, u]^T$  using the following approach.

**Case:**  $\xi = x/t \leq u_*$

In this situation there are two cases:

- left shock:  $A_* > A_L$ , where it is computed

$$\mathbf{W}(\xi) = \begin{cases} [A_*, u_*]^T & \text{if } S_L \leq \xi \leq u_* \\ [A_L, u_L]^T & \text{if } S_L > \xi \end{cases}, \quad (13)$$

- left rarefaction:  $A_* \leq A_L$ , where it is computed

$$\mathbf{W}(\xi) = \begin{cases} [A_L, u_L]^T & \text{if } \xi \leq u_L - c_L \\ [\hat{A}_L, \hat{u}_L]^T & \text{if } u_L - c_L < \xi \leq u_* - c_* \\ [A_*, u_*]^T & \text{if } u_* \geq \xi > u_* - c_* \end{cases}, \quad (14)$$

where  $[\hat{A}_L, \hat{u}_L]$  are computed from

$$\hat{u}_L = \frac{1}{5} \left( u_L + 4c_L + 4\frac{x}{t} \right), \quad \hat{c}_L = \hat{u}_L - \frac{x}{t}. \quad (15)$$

**Case:**  $\xi = x/t > u_*$

In this situation there are two cases:

- right shock:  $A_* > A_R$ , where it is computed

$$\mathbf{W}(\xi) = \begin{cases} [A_*, u_*]^T & \text{if } u_* < \xi \leq S_R \\ [A_R, u_R]^T & \text{if } \xi > S_R \end{cases}, \quad (16)$$

- right rarefaction:  $A_* \leq A_R$ , where it is computed

$$\mathbf{W}(\xi) = \begin{cases} [A_R, u_R]^T & \text{if } \xi > u_R + c_R \\ [\hat{A}_R, \hat{u}_R]^T & \text{if } u_* + c_* \leq \xi \leq u_R + c_R \\ [A_*, u_*]^T & \text{if } \xi < u_* + c_* \end{cases}, \quad (17)$$

where  $[\hat{A}_R, \hat{u}_R]$  are computed as

$$\hat{u}_R = \frac{1}{5} \left( u_R - 4c_R + 4\frac{x}{t} \right), \quad \hat{c}_R = -\hat{u}_R + \frac{x}{t}. \quad (18)$$

## 2.2 Numerical Methods

Solutions to system (1) must be approximated using numerical methods. Both a first order method and the second order MUSCL-Hancock method have been adopted. Several steps are required to resolve the model equations across the entire vascular network. Initially, discretization of each spatial and temporal domain is necessary to create control volumes over which the quasi-linear form of the systems are defined. Subsequently, boundary conditions must be applied at the inlet and outlets of the network, while junction coupling conditions need to be imposed at bifurcations.

### 2.2.1 Space and time discretization

The spatial domain  $[a, b]$  is discretized using  $M$  computational cells of equal length  $\Delta x = \frac{b-a}{M}$ . The  $i$ -th computational cell is denoted by  $I_i = [x_{i-\frac{1}{2}}, x_{i+\frac{1}{2}}]$ , where  $i = 1, \dots, M$ , and  $x_{i-\frac{1}{2}} = x_i - \frac{\Delta x}{2}$  and  $x_{i+\frac{1}{2}} = x_i + \frac{\Delta x}{2}$  denote its left and right interfaces. The time domain  $[0, t_{\text{end}}]$  is discretized in intervals denoted by  $T^n = [t^n, t^{n+1}]$ , where the time step  $\Delta t^n = t^{n+1} - t^n$  is computed as  $\Delta t^n = \text{CFL} \frac{\Delta x}{\text{eigMax}(n)}$ , where  $\text{CFL} = 0.9$  is the *Courant-Friedrichs-Levy number*, and  $\text{eigMax}(n)$  is the eigenvalue with maximum absolute value at time step  $t^n$ . The control volume for the discretization of (6) is therefore  $V_i = I_i \times T^n = [x_{i-\frac{1}{2}}, x_{i+\frac{1}{2}}] \times [t^n, t^{n+1}]$ .

### 2.2.2 First order scheme

We adopted a finite volume method of the form

$$\mathbf{Q}_i^{n+1} = \mathbf{Q}_i^n - \frac{\Delta t}{\Delta x} \left[ \mathbf{F}_{i+\frac{1}{2}} - \mathbf{F}_{i-\frac{1}{2}} \right] + \Delta t \mathbf{S}_i \quad i = 1, \dots, M , \quad (19)$$

where  $M$  is the number of computational cells. Finite volume schemes of the form (19) are derived through the integration of the equations from system (5) across the control volume  $V_i$ , and by introducing suitable approximations for the integral averages arising from the integration. In particular  $\mathbf{Q}_i^{n+1}$  and  $\mathbf{Q}_i^n$  are approximations of spatial averages,  $\mathbf{F}_{i\pm\frac{1}{2}}$  are approximations of temporal averages and  $\mathbf{S}_i$  is an approximation of space-time average:

$$\mathbf{Q}_i^n \approx \frac{1}{\Delta x} \int_{x_{i-1/2}}^{x_{i+1/2}} \mathbf{Q}(x, t^n) dx, \quad \mathbf{F}_{i\pm\frac{1}{2}} \approx \frac{1}{\Delta t} \int_{t^n}^{t^{n+1}} \mathbf{F}(\mathbf{Q}(x_{i\pm\frac{1}{2}}, t)) dt, \quad \mathbf{S}_i = \frac{1}{\Delta x} \frac{1}{\Delta t} \int_{x_{i-1/2}}^{x_{i+1/2}} \int_{t^n}^{t^{n+1}} \mathbf{S}(\mathbf{Q}(x, t)) dt dx.$$

### 2.2.3 HLL numerical flux (Harten et al. 1983)

The HLL numerical flux is defined as

$$\mathbf{F}_{i+\frac{1}{2}}^{HLL}(\mathbf{Q}_L, \mathbf{Q}_R) = \begin{cases} \mathbf{F}_L & \text{if } 0 \leq S_L, \\ \mathbf{F}_0 = \frac{S_R \mathbf{F}_L - S_L \mathbf{F}_R + S_L S_R (\mathbf{Q}_R - \mathbf{Q}_L)}{S_R - S_L} & \text{if } S_L < 0 < S_R, \\ \mathbf{F}_R & \text{if } S_R \leq 0, \end{cases} \quad (20)$$

where  $\mathbf{F}_K = \mathbf{F}(\mathbf{Q}_K)$  for  $K \in \{L, R\}$ . To compute the fastest left and right travelling waves  $S_L$  and  $S_R$ , the *Two rarefaction (TR) Riemann Problem solver* is used. Assuming that both waves associated with genuinely non linear characteristic fields are rarefactions, it is possible to compute  $A_*^{TR} = \left( \frac{2\rho}{\beta} \right)^2 (c_*^{TR})^4$ , where  $c_*^{TR} = \frac{1}{2}(c_L + c_R) - \frac{1}{8}(u_R - u_L)$ . Then  $S_L$  and  $S_R$  can be computed as

$$S_L = \begin{cases} u_L - c_L & \text{if } A_*^{TR} \leq A_L, \\ u_L - \frac{M_L}{A_L} & \text{if } A_*^{TR} > A_L, \end{cases} \quad S_R = \begin{cases} u_R + c_R & \text{if } A_*^{TR} \leq A_R, \\ u_R + \frac{M_R}{A_R} & \text{if } A_*^{TR} > A_R, \end{cases} \quad (21)$$

where  $d = \frac{\beta}{3\rho}$  and

$$M_K = \left( \frac{d A_*^{TR} A_K \left( (A_*^{TR})^{3/2} - (A_K)^{3/2} \right)}{A_*^{TR} - A_K} \right)^{1/2}, \quad K \in \{L, R\}. \quad (22)$$

## 2.2.4 MUSCL-Hancock (MH) scheme (Leer 1979)

The discretization of system (1) can be achieved using the MH scheme with ENO reconstruction. This approach ensures second-order accuracy in both space and time through the computation of the intercell flux  $\mathbf{F}_{i+\frac{1}{2}}$  according to the following steps as made in (Ghitti et al. 2023):

1. Data reconstruction and cell boundary values: based on the cell averages  $\mathbf{Q}_i^n$ , a first-degree reconstruction polynomial vector  $\mathbf{P}_i(x)$  is obtained for each cell  $I_i$  as

$$\mathbf{P}_i(x) = \mathbf{Q}_i^n + (x - x_i)\Delta_i, \quad (23)$$

where  $\Delta_i$  is the slope computed using the ENO criterion. The boundary extrapolated values are computed as

$$\mathbf{Q}_i^L = \mathbf{P}_i\left(x_{i-\frac{1}{2}}\right), \quad \mathbf{Q}_i^R = \mathbf{P}_i\left(x_{i+\frac{1}{2}}\right). \quad (24)$$

2. Evolution of boundary extrapolated values by  $\frac{\Delta t}{2}$ : the *evolution step* is computed as:

$$\overline{\mathbf{Q}}_i^L = \mathbf{Q}_i^L - \frac{1}{2} \frac{\Delta t}{\Delta x} (\mathbf{F}(\mathbf{Q}_i^R) - \mathbf{F}(\mathbf{Q}_i^L)) + \frac{1}{2} \Delta t \mathbf{S}(\mathbf{Q}_i^L), \quad \overline{\mathbf{Q}}_i^R = \mathbf{Q}_i^R - \frac{1}{2} \frac{\Delta t^n}{\Delta x} (\mathbf{F}(\mathbf{Q}_i^R) - \mathbf{F}(\mathbf{Q}_i^L)) + \frac{1}{2} \Delta t \mathbf{S}(\mathbf{Q}_i^R). \quad (25)$$

3. Solving a classical Riemann problem at  $x_{i+\frac{1}{2}}$ : the classical Riemann problem reads:

$$\begin{aligned} \partial_t \mathbf{Q} + \partial_x \mathbf{F}(\mathbf{Q}) &= 0 \\ \mathbf{Q}(x, t^n) &= \begin{cases} \overline{\mathbf{Q}}_i^R, & \text{if } x < x_{i+\frac{1}{2}} \\ \overline{\mathbf{Q}}_{i+1}^L, & \text{if } x > x_{i+\frac{1}{2}} \end{cases} \end{aligned} \quad (26)$$

The solution of (26) is  $\mathbf{Q}_{i+\frac{1}{2}}\left(\frac{x-x_{i+\frac{1}{2}}}{t-t^n}\right)$ , using which it is possible to compute the numerical flux as

$$\mathbf{F}_{i+\frac{1}{2}} = \mathbf{F}\left(\mathbf{Q}_{i+\frac{1}{2}}(0)\right). \quad (27)$$

In this report the HLL approximate Riemann solver is adopted to solve the Riemann problem.

To compute the numerical source it is sufficient to proceed as follows:

$$\mathbf{S}_i = \mathbf{S}\left(\mathbf{Q}_i^n + \frac{1}{2} \Delta t^n [-\mathbf{A}(\mathbf{Q}_i^n) \Delta_i + \mathbf{S}(\mathbf{Q}_i^n)]\right), \quad (28)$$

which is obtained by approximating the volume-integral average of the source term  $\mathbf{S}(\mathbf{Q}(x, t))$  by using the midpoint rule in space and time, where the midpoint value  $\mathbf{Q}(x_i, \frac{\Delta t^n}{2})$  is computed by performing a Taylor expansion in time and applying the Cauchy–Kowalevski method at point  $x_i$ .

## 2.3 Boundary conditions

Boundary conditions must be prescribed at both the inlet and outlet of each arterial domain. These conditions are categorized into *inlet*, *junction*, and *terminal boundary* conditions. To compute the numerical fluxes at the boundary of the domain, it is necessary to define the states  $\mathbf{Q}_L^{BC}$  and  $\mathbf{Q}_R^{BC}$ .

In fact, let us consider a 1D domain and divide it into  $M$  computational cells numbered from 1 to  $M$ . We now consider (19) and note that for  $i = 1$  and for  $i = M$  there is the problem of the value of  $\mathbf{F}_{1/2}$  and  $\mathbf{F}_{M+1/2}$ , which are undefined. To solve this indefiniteness problem, we impose

$$\mathbf{F}_{1/2} = \mathbf{F}(\mathbf{Q}_L^{BC}) \quad \mathbf{F}_{M+1/2} = \mathbf{F}(\mathbf{Q}_R^{BC}). \quad (29)$$

Depending on the behaviour at the boundary of the domain we want,  $\mathbf{Q}_L^{BC}$  and  $\mathbf{Q}_R^{BC}$  will be defined.

### 2.3.1 Inflow boundary conditions

The flow  $Q_L^{BC} = Q_{in}(t)$  is imposed at the inlet of the domain, i.e. at the root of the network, and it is taken from (Xiao et al. 2014), courtesy of the authors of the paper. The area at the inlet  $A_L^{BC}$  is computed by solving the following non linear equation, obtained using the Riemann invariant associated to the  $\lambda_2$ -characteristic field:

$$\frac{Q_L^{BC}}{A_L^{BC}} - \frac{Q_{1D}}{A_{1D}} + 4c(A_{1D}) - 4c(A_L^{BC}) = 0, \quad (30)$$

where for the first order scheme it is used  $\mathbf{Q}_{1D} = \mathbf{Q}_1^n$ , while for the MH scheme it is used  $\mathbf{Q}_{1D} = \overline{\mathbf{Q}}_1^L$ , as computed in (25).

### 2.3.2 Terminal boundary conditions

The simulation of the impact of peripheral resistance involves employing linear lumped parameter models coupled to 1D model terminal branches. As shown in [Figure 1](#), the RCR Windkessel model comprises a resistance  $R_p$  connected in series with a parallel combination of a second resistance  $R_d$  and a compliance  $C$ .

In the RCR model, the terminal flow  $Q_R^{BC} = \frac{P(A_R^{BC}) - P_C}{R_p}$  is imposed in the relation given by the Riemann invariant,  $\frac{Q_R^{BC}}{A_R^{BC}} - \frac{Q_{1D}}{A_{1D}} + 4c(A_R^{BC}) - 4c(A_{1D}) = 0$ . Solving the resulting non linear equation the state vector  $\mathbf{Q}_R^{BC}$  is obtained, then the pressure evolves as:

$$\frac{dP_C}{dt} = \frac{1}{C} \left( Q_R^{BC} - \frac{P_C - P_d}{R_d} \right).$$

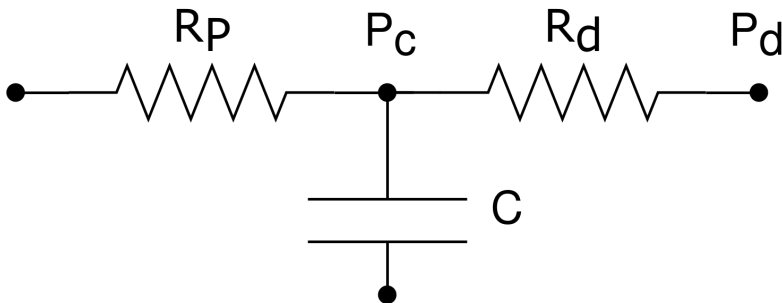


**Figure 1:** RCR Windkessel model diagram.

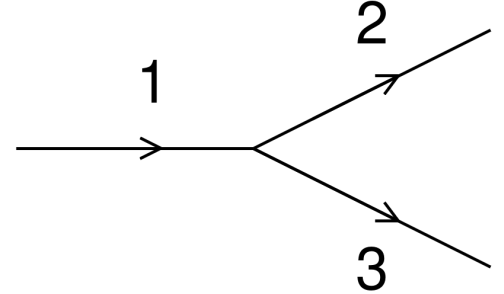


**Figure 2:** A 3 vessels junction.

### 2.3.3 Junction coupling conditions

In the context of the 1D formulation, it is important to ensure the enforcement of coupling conditions between arterial domains and junctions. The nodes connecting each segment are treated as discontinuities in this context. The set of coupling equations includes the principles of mass conservation, total pressure continuity and conservation of generalised Riemann invariants. Analysing a junction with three converging vessels, as illustrated in [Figure 2](#), the resulting system of equations can be outlined as follows:

$$\begin{cases} Q_*^{(1)} - Q_*^{(2)} - Q_*^{(3)} = 0 \\ P_*^{(1)} + \frac{\rho}{2} \left( u_*^{(1)} \right)^2 = P_*^{(2)} + \frac{\rho}{2} \left( u_*^{(2)} \right)^2 \\ P_*^{(1)} + \frac{\rho}{2} \left( u_*^{(1)} \right)^2 = P_*^{(3)} + \frac{\rho}{2} \left( u_*^{(3)} \right)^2 \\ u_*^{(1)} - u_{1D}^{(1)} + 4c_*^{(1)} - 4c_{1D}^{(1)} = 0 \\ u_*^{(k)} - u_{1D}^{(k)} - 4c_*^{(k)} + 4c_{1D}^{(k)} = 0 \quad k = 2, 3 \end{cases}. \quad (31)$$

## 2.4 Empirical convergence rate

The *empirical convergence rate* refers to the observed rate at which a numerical method approaches the exact solution as the grid size decreases. In the setting considered, let  $M$  be the number of computational cells within a mesh  $\mathcal{M}$  and let  $l$  be the length of the 1D-domain. The mesh size then is given by  $\Delta x = \frac{l}{M}$ .

The exact solution is obtained with the method of *manufactured solutions*. It consists of inserting in (5) a smooth function  $\bar{\mathbf{Q}}(x, t)$ . Since the latter will not necessarily satisfy (5), one obtains

$$\partial_t \bar{\mathbf{Q}} + \partial_x \mathbf{F}(\bar{\mathbf{Q}}) - \mathbf{S}(\bar{\mathbf{Q}}) = \mathbf{S}_{new}(\bar{\mathbf{Q}}). \quad (32)$$

The function  $\bar{\mathbf{Q}}$  is the exact solution of the new balance law

$$\partial_t \mathbf{Q} + \partial_x \mathbf{F}(\mathbf{Q}) = \bar{\mathbf{S}}(\mathbf{Q}), \quad (33)$$

where  $\bar{\mathbf{S}}(\mathbf{Q}) = \mathbf{S}(\mathbf{Q}) + \mathbf{S}_{new}(\mathbf{Q})$ . Therefore, equation (33) is used to test the empirical convergence rate, as we now have the exact solution. The smooth function considered is the following:

$$A(x, t) = r_0^2 \pi + \frac{1}{10} r_0^2 \pi \sin \left( \frac{2\pi}{L} x \right) \cos \left( \frac{2\pi}{T_0} t \right) \quad Q(x, t) = \tilde{q} - \frac{1}{10} \frac{L}{T_0} r_0^2 \pi \cos \left( \frac{2\pi}{L} x \right) \sin \left( \frac{2\pi}{T_0} t \right), \quad (34)$$

where:  $r_0 = 0.999\text{cm}$ ,  $L = 100\text{cm}$ ,  $T_0 = 1\text{s}$ ,  $\tilde{q} = 0\text{ml/s}$ .

Denoting  $\tilde{\mathbf{Q}}_i$  and  $\mathbf{Q}_i$  as the state vectors of the numerical solution and the exact solution respectively, at time  $t_{end}$  within the  $i$ -th computational cell, where  $i = 1, \dots, M$ , the  $l_1$ ,  $l_2$  and  $l_\infty$  norms of the error are computed as follows

$$e_1(\mathcal{M}) = \Delta x \sum_{i=1}^M \left| \mathbf{Q}_i - \tilde{\mathbf{Q}}_i \right|, \quad e_2(\mathcal{M}) = \sqrt{\Delta x \sum_{i=1}^M \left| \mathbf{Q}_i - \tilde{\mathbf{Q}}_i \right|^2}, \quad e_\infty(\mathcal{M}) = \max_i \left| \mathbf{Q}_i - \tilde{\mathbf{Q}}_i \right|. \quad (35)$$

When examining two distinct meshes, denoted as  $\mathcal{M}_1$  and  $\mathcal{M}_2$ , with  $\mathcal{M}_1$  having a larger mesh size compared to  $\mathcal{M}_2$ , the empirical convergence rates  $p_1$ ,  $p_2$ , and  $p_\infty$  for the error norms  $l_1$ ,  $l_2$ , and  $l_\infty$ , respectively, are determined as

$$p_1 = \frac{\log \left( \frac{e_1(\mathcal{M}_2)}{e_1(\mathcal{M}_1)} \right)}{\log \left( \frac{\Delta x^{(\mathcal{M}_2)}}{\Delta x^{(\mathcal{M}_1)}} \right)}, \quad p_2 = \frac{\log \left( \frac{e_2(\mathcal{M}_2)}{e_2(\mathcal{M}_1)} \right)}{\log \left( \frac{\Delta x^{(\mathcal{M}_2)}}{\Delta x^{(\mathcal{M}_1)}} \right)}, \quad p_\infty = \frac{\log \left( \frac{e_\infty(\mathcal{M}_2)}{e_\infty(\mathcal{M}_1)} \right)}{\log \left( \frac{\Delta x^{(\mathcal{M}_2)}}{\Delta x^{(\mathcal{M}_1)}} \right)}. \quad (36)$$

## 2.5 Assessment of computational errors

Consider a sequence of meshes denoted as  $\{\mathcal{M}_1, \dots, \mathcal{M}_N\}$ , each comprising a number of computational cells given by  $M = \max \left\{ \left\lceil \frac{l}{\Delta x_r} \right\rceil, 2 \right\}$ , where  $\Delta x_r = 2^{-(r-1)} \Delta x_1$  with  $r = 2, \dots, M$ . The relative errors of the 1D solutions concerning the 3D simulations, as detailed in (Xiao et al. 2014), are computed as

$$\varepsilon_{P,\text{avg}} = \frac{1}{N_t} \sum_{i=1}^{N_t} \left| \frac{P_i^{1D} - P_i^{3D}}{P_i^{3D}} \right|, \quad \varepsilon_{Q,\text{avg}} = \frac{1}{N_t} \sum_{i=1}^{N_t} \left| \frac{Q_i^{1D} - Q_i^{3D}}{\max_j(Q_j^{3D})} \right|, \quad (37)$$

$$\varepsilon_{P,\text{max}} = \max_i \left| \frac{P_i^{1D} - P_i^{3D}}{P_i^{3D}} \right|, \quad \varepsilon_{Q,\text{max}} = \max_i \left| \frac{Q_i^{1D} - Q_i^{3D}}{\max_j(Q_j^{3D})} \right|, \quad (38)$$

$$\varepsilon_{P,\text{sys}} = \frac{\max_i(P_i^{1D}) - \max_i(P_i^{3D})}{\max_i(P_i^{3D})}, \quad \varepsilon_{Q,\text{sys}} = \frac{\max_i(Q_i^{1D}) - \max_i(Q_i^{3D})}{\max_i(Q_i^{3D})}, \quad (39)$$

$$\varepsilon_{P,\text{dias}} = \frac{\min_i(P_i^{1D}) - \min_i(P_i^{3D})}{\min_i(P_i^{3D})}, \quad \varepsilon_{Q,\text{dias}} = \frac{\min_i(Q_i^{1D}) - \min_i(Q_i^{3D})}{\min_i(Q_i^{3D})}, \quad (40)$$

at given spatial locations and time points, denoted by  $i = 1, \dots, n$ , where  $P_i^{1D}$  and  $Q_i^{1D}$  represent solutions obtained from the 1D simulation. Correspondingly, at the same spatial location and time point  $i$ ,  $P_i^{3D}$  and  $Q_i^{3D}$  stand for the cross-sectional averaged pressure and flow from the 3D model.

The use of these error metric allows for an easy comparison of the results, since are also used in (Xiao et al. 2014).

## 2.6 Modeling of endoleak and endograft

The most common aneurysm is the Abdominal Aortic Aneurism (AAA), typically in the infrarenal region, while the second most common is the Thoracic Aortic Aneurism (TAA) (Davis et al. 2014). We simulate the presence of a thoracic stent since the scientific literature is rich in studies on this aortic tract, making it easier to compare the results obtained. To simulate the stent in the thoracic aorta (called TAS from now on), a thoracic tract 15.2cm long is considered. This length is chosen both because it is in agreement with the scientific literature, such as (Xue et al. 2020), but also because it is similar to the scientific literature used later for the comparison of the results on the impact on hemodynamics.

Although there is disagreement on the precise value, stent oversizing is considered safe in the range from 10% to 20% (Prehn et al. 2009), so we decided to simulate an oversizing of 15%, obtained by increasing the radius of the stented tract by 15%. To simulate the effect of increased tube stiffness due to the stent, the wave speed is changed, increasing it by 10%, 25% and 35%. The relation between the stiffness  $K$  (see equation (4)) and the wave speed  $c$  can be deduced by the definition of  $c$  and  $\beta$  written in Section 2.1.2.

For this task, all simulations were done using the second-order method, with a  $\text{dx} = 0.25$  (using the notation of Section 3.2) and employing data from the 20th cardiac cycle, where convergence to periodicity was achieved. The solution approximation where there is no increase in wave speed is called “reference” to follow; note that this case corresponds to the approximation obtained in Section 3.2.

To calculate the pulse wave velocity (PWV), the length of the aorta is divided by the difference between the minimum peak time of the pressure curve at the base (i.e., where the flow is imposed) and at the end of the aorta (i.e., at the connection with the iliac arteries).

### 3 Results

All results are obtained with a custom-made laptop computer with the following components: Intel Core i7 13700H (14 Cores), 64 GB ( $2 \times 32$  GB) 3200 MHz DDR4 Corsair, NVIDIA GeForce RTX 3050 (RAM 4 GB GDDR6, DirectX 12.1).

#### 3.1 Task 1 - Empirical convergence rates

Two identical vessels with identical geometrical and mechanical attributes interconnected at both ends are considered. The properties of the vessels are shown in [Table 1](#).

**Table 1:** Properties of vessels used in the empirical convergence rate ([Section 3.1](#)).

Property	Value used	Property	Value used
Length	12.0685 cm	Wall thickness	0.11 cm
Inlet radius	1.2 cm	Blood density	$1000 \text{ g/cm}^3$
Outlet radius	1.2 cm	Blood viscosity	0
Wavespeed	500.0 cm/s	Velocity profile order, $\delta$	2
Initial flow velocity	0	Young's modulus	$4 \cdot 10^{-5} \text{ Pa}$
Initial pressure	0	Reference pressure	0
External pressure	0		

The convergence rates outlined in [Section 2.4](#) are used for analysis, both the first order and MH schemes with HLL Riemann problem solver are used. As expected from identical vessels, equal results are obtained for both, so only the results for a single vessel are shown.

In [Figure 3](#) and [Figure 4](#), it is shown the convergence of the approximations of the solution when doubling the sampling rate, for the first-order method and for the MH scheme.

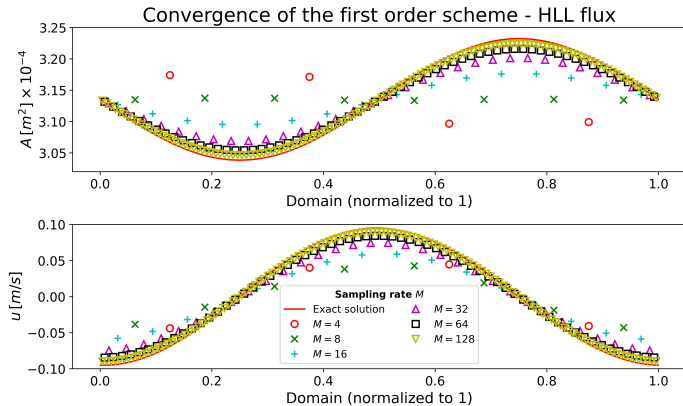


**Figure 3:** Convergence of the HLL flux for different sampling rate, case of two identical connected vessels.

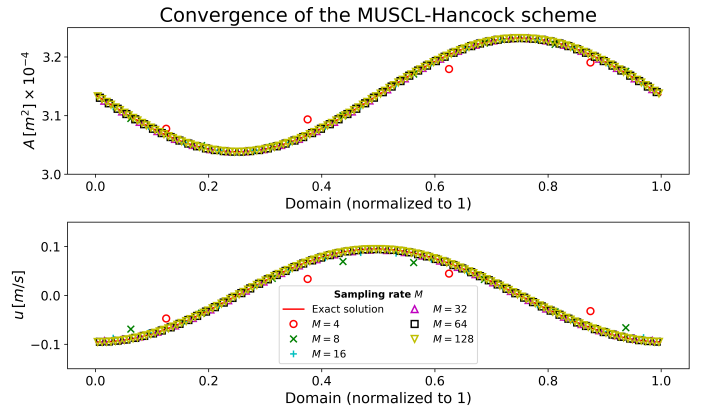


**Figure 4:** Convergence of the MH scheme for different sampling rate, case of two identical connected vessels.

In [Table 2](#) and [Table 3](#) the error norms, empirical convergence rates and CPU time are reported for the first order method, while for the second order method they are reported in [Table 4](#) and [Table 5](#).

As notation, an apostrophe "A" is employed to denote the error and convergence rate of the *area*, whereas an apostrophe "q" is utilized for the convergence rate of the *flow*. For simplicity, the tables feature a slightly different notation from what was discussed in [Section 2.4](#): the error norm is expressed in terms of the number of discretization steps rather than the mesh.

**Table 2:** Area vector: CPU time, errors and convergence rates ( $l_1$ ,  $l_2$ ,  $l_\infty$  norms). First-order method is used to approximate the solution for various discretization step counts  $M$ .

M	$e_1^A(M)$	$p_1^A(M)$	$e_2^A(M)$	$p_2^A(M)$	$e_\infty^A(M)$	$p_\infty^A(M)$	tCpu
8	$6.3919 \times 10^{-6}$	0.7290	$6.9223 \times 10^{-6}$	0.6141	$9.1654 \times 10^{-6}$	0.2276	0.0441 s
16	$3.5896 \times 10^{-6}$	0.8324	$3.9617 \times 10^{-6}$	0.8051	$5.5312 \times 10^{-6}$	0.7286	0.1408 s
32	$1.9506 \times 10^{-6}$	0.8799	$2.1625 \times 10^{-6}$	0.8734	$3.0659 \times 10^{-6}$	0.8513	0.1492 s
64	$1.0172 \times 10^{-6}$	0.9393	$1.1292 \times 10^{-6}$	0.9374	$1.6265 \times 10^{-6}$	0.9145	0.5161 s
128	$5.2005 \times 10^{-7}$	0.9679	$5.7747 \times 10^{-7}$	0.9675	$8.3891 \times 10^{-7}$	0.9552	1.9841 s

**Table 3:** Flow vector: CPU time, errors and convergence rates ( $l_1$ ,  $l_2$ ,  $l_\infty$  norms). First-order method is used to approximate the solution for various discretization step counts  $M$ .

M	$e_1^q(M)$	$p_1^q(M)$	$e_2^q(M)$	$p_2^q(M)$	$e_\infty^q(M)$	$p_\infty^q(M)$	tCpu
8	$1.0517 \times 10^{-5}$	-0.4319	$1.1396 \times 10^{-5}$	-0.5434	$1.5583 \times 10^{-5}$	-0.8842	0.0441 s
16	$7.1737 \times 10^{-6}$	0.5519	$7.9230 \times 10^{-6}$	0.5244	$1.1176 \times 10^{-5}$	0.4795	0.1408 s
32	$4.0595 \times 10^{-6}$	0.8214	$4.5038 \times 10^{-6}$	0.8149	$6.3775 \times 10^{-6}$	0.8094	0.1492 s
64	$2.1162 \times 10^{-6}$	0.9398	$2.3511 \times 10^{-6}$	0.9378	$3.3312 \times 10^{-6}$	0.9369	0.5161 s
128	$1.0778 \times 10^{-6}$	0.9733	$1.1983 \times 10^{-6}$	0.9723	$1.7002 \times 10^{-6}$	0.9704	1.9841 s

**Table 4:** Area vector: CPU time, errors and convergence rates ( $l_1$ ,  $l_2$ ,  $l_\infty$  norms). Second-order method is used to approximate the solution for various discretization step counts  $M$ .

M	$e_1^A(M)$	$p_1^A(M)$	$e_2^A(M)$	$p_2^A(M)$	$e_\infty^A(M)$	$p_\infty^A(M)$	tCpu
8	$2.2925 \times 10^{-7}$	3.0360	$2.4532 \times 10^{-7}$	3.0296	$3.2527 \times 10^{-7}$	3.0433	0.0917 s
16	$5.0227 \times 10^{-8}$	2.1904	$6.4264 \times 10^{-8}$	1.9326	$1.5043 \times 10^{-7}$	1.1125	0.1864 s
32	$9.6803 \times 10^{-9}$	2.3753	$1.2822 \times 10^{-8}$	2.3254	$3.2091 \times 10^{-8}$	2.2289	0.3727 s
64	$2.4935 \times 10^{-9}$	1.9569	$3.3812 \times 10^{-9}$	1.9230	$7.0626 \times 10^{-9}$	2.1839	1.4079 s
128	$6.3648 \times 10^{-10}$	1.9700	$8.8765 \times 10^{-10}$	1.9295	$2.0491 \times 10^{-9}$	1.7852	5.4485 s

**Table 5:** Flow vector: CPU time, errors and convergence rates ( $l_1$ ,  $l_2$ ,  $l_\infty$  norms). Second-order method is used to approximate the solution for various discretization step counts  $M$ .

M	$e_1^q(M)$	$p_1^q(M)$	$e_2^q(M)$	$p_2^q(M)$	$e_\infty^q(M)$	$p_\infty^q(M)$	tCpu
8	$3.4804 \times 10^{-6}$	1.3264	$4.4767 \times 10^{-6}$	1.0007	$6.5972 \times 10^{-6}$	0.7203	0.0917 s
16	$9.9770 \times 10^{-7}$	1.8026	$1.2069 \times 10^{-6}$	1.8912	$2.0906 \times 10^{-6}$	1.6579	0.1864 s
32	$2.1697 \times 10^{-7}$	2.2011	$2.7777 \times 10^{-7}$	2.1193	$5.3560 \times 10^{-7}$	1.9647	0.3727 s
64	$5.2882 \times 10^{-8}$	2.0366	$6.8308 \times 10^{-8}$	2.0238	$1.3418 \times 10^{-7}$	1.9970	1.4079 s
128	$1.2983 \times 10^{-8}$	2.0262	$1.6885 \times 10^{-8}$	2.0163	$3.3543 \times 10^{-8}$	2.0000	5.4485 s

### 3.2 Task 2 - Modelling blood flow in the arterial network used in (Xiao et al. 2014)

Data from (Xiao et al. 2014), provided by the authors, were used to perform this task. Precisely, the same flow was prescribed at the inlet of the aorta and the same arterial network was recreated (the details of which are given in the article in Table IV) using what was explained in Section 2.3. An important difference from the article is that the mechanical and geometrical properties were kept constant: the average of the radii and inlet and outlet velocities from the article was used. Results are shown for three different arteries, placed in different positions to illustrate the behaviour of the model used in different situations. The same abbreviations used by (Xiao et al. 2014) are used for the results.

We generated the results in Figure 5 after the solution converged to periodicity, which in the case studied occurs at the 20th cardiac cycle. In fact, at the 20th cycle there is less than 5 per cent change in the  $l_2$ ,  $l_1$ ,  $l_\infty$  norms compared to the previous cycle for all vessels. Refinement of the mesh is then stopped when the errors obtained have changed by less than 5 per cent for all vessels.

The average values of flows and pressures are shown in table Table 6.

**Table 6:** Averages of flows and pressures of the curves in Figure 5.

		AO	BC	LCCA	LSUB	SMA	RRE	IMA	RIL
Pressure (mmHg)	Replicated 1D	90.04	90.16	90.15	90.11	89.39	88.76	89.50	90.08
	Xiao 1D	90.36	90.47	90.45	90.36	88.81	87.82	88.81	90.07
	Xiao 3D	90.83	90.90	90.92	90.78	88.49	87.32	89.44	90.69
Flow (mL/s)	Replicated 1D	104.94	10.90	2.24	8.67	16.57	13.49	2.25	11.37
	Xiao 1D	102.72	10.84	2.23	8.60	16.32	13.29	2.21	11.15
	Xiao 3D	102.81	10.89	2.24	8.64	16.26	13.22	2.22	11.23

**Table 7**, **Table 8** and **Table 9** show the errors of the three chosen arteries to mesh refinement. To calculate the error, the solution arrived at convergence is considered and it is interpolated on the time vector of the 3D solution reported by (Xiao et al. 2014). See Section 2.4 and Section 2.5 and for details on errors and notation.

In Figure 6 only the efficiency plots of the brachiocephalic artery are given since for the other arteries something very similar is obtained.

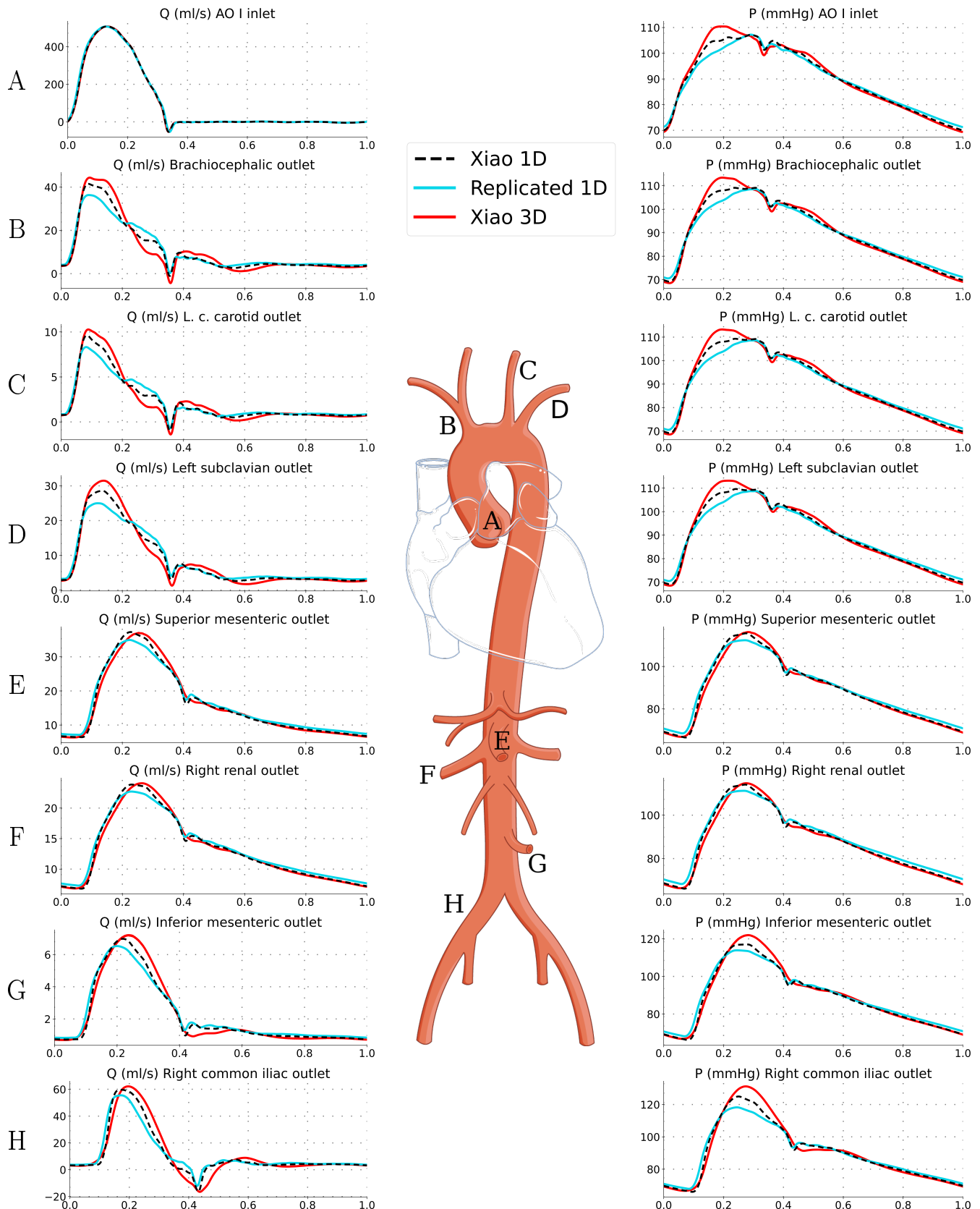


**Figure 5:** Full aorta case. Flow rate (left) and pressure (right) with time normalised to 1 second in eight outlets in the 3D model of (Xiao et al. 2014), in the 1D model of (Xiao et al. 2014) and in the results obtained from the model used in this work. The central image of the aorta is taken from ([Commons 2024](#)).

**Table 7:** Errors in the approximate solution in the brachiocephalic artery for different mesh refinements.

dx	order	$\epsilon_{P,avg}$	$\epsilon_{P,max}$	$\epsilon_{P,sys}$	$\epsilon_{P,dias}$	$\epsilon_{Q,avg}$	$\epsilon_{Q,max}$	$\epsilon_{Q,sys}$	$\epsilon_{Q,dias}$	tCpu
0.25	1	2.82e-02	9.20e-02	-4.30e-02	2.95e-02	6.97e-02	2.52e-01	-1.82e-01	1.10e-01	5408 s
0.5	1	2.83e-02	9.20e-02	-4.34e-02	2.98e-02	6.89e-02	2.49e-01	-1.78e-01	1.13e-01	4691 s
1.0	1	3.22e-02	9.28e-02	-4.44e-02	3.07e-02	6.93e-02	2.37e-01	-1.70e-01	1.25e-01	2090 s
2.0	1	3.23e-02	9.19e-02	-4.60e-02	3.20e-02	6.75e-02	2.27e-01	-1.63e-01	1.44e-01	2027 s
0.25	2	2.83e-02	9.21e-02	-4.27e-02	2.93e-02	6.99e-02	2.53e-01	-1.82e-01	1.05e-01	6612 s
0.5	2	2.83e-02	9.21e-02	-4.29e-02	2.95e-02	6.93e-02	2.52e-01	-1.78e-01	1.04e-01	2653 s
1.0	2	3.23e-02	9.36e-02	-4.31e-02	2.98e-02	7.00e-02	2.42e-01	-1.71e-01	1.04e-01	2287 s
2.0	2	3.23e-02	9.37e-02	-4.33e-02	3.05e-02	6.93e-02	2.39e-01	-1.64e-01	1.10e-01	2300 s
(Xiao et al. 2014)		2.06e-02	7.54e-02	-4.76e-02	-0.99e-02	4.94e-02	21.5e-02	-4.07e-02	0.32e-02	

**Table 8:** Errors in the approximate solution in the superior mesenteric artery for different mesh refinements.

dx	order	$\epsilon_{P,avg}$	$\epsilon_{P,max}$	$\epsilon_{P,sys}$	$\epsilon_{P,dias}$	$\epsilon_{Q,avg}$	$\epsilon_{Q,max}$	$\epsilon_{Q,sys}$	$\epsilon_{Q,dias}$	tCpu
0.25	1	2.33e-02	5.46e-02	-3.32e-02	2.54e-02	3.00e-02	9.66e-02	-5.69e-02	2.13e-02	5408 s
0.5	1	2.34e-02	5.46e-02	-3.30e-02	2.62e-02	3.00e-02	9.65e-02	-5.74e-02	2.14e-02	4691 s
1.0	1	2.73e-02	5.61e-02	-3.26e-02	2.86e-02	3.21e-02	8.75e-02	-5.96e-02	2.14e-02	2090 s
2.0	1	2.77e-02	5.65e-02	-3.20e-02	3.23e-02	3.15e-02	8.64e-02	-6.29e-02	2.14e-02	2027 s
0.25	2	2.34e-02	5.58e-02	-3.33e-02	2.46e-02	3.02e-02	9.70e-02	-5.59e-02	2.10e-02	6612 s
0.5	2	2.35e-02	5.73e-02	-3.33e-02	2.49e-02	3.03e-02	9.73e-02	-5.54e-02	2.09e-02	2653 s
1.0	2	2.74e-02	5.62e-02	-3.32e-02	2.56e-02	3.25e-02	8.77e-02	-5.48e-02	2.06e-02	2287 s
2.0	2	2.77e-02	5.65e-02	-3.31e-02	2.75e-02	3.26e-02	8.91e-02	-5.40e-02	2.02e-02	2300 s
(Xiao et al. 2014)		2.06e-02	7.54e-02	-4.76e-02	-0.99e-02	4.94e-02	21.5e-02	-4.07e-02	0.32e-02	

**Table 9:** Errors in the approximate solution in the right iliac artery for different mesh refinements.

dx	order	$\epsilon_{P,avg}$	$\epsilon_{P,max}$	$\epsilon_{P,sys}$	$\epsilon_{P,dias}$	$\epsilon_{Q,avg}$	$\epsilon_{Q,max}$	$\epsilon_{Q,sys}$	$\epsilon_{Q,dias}$	tCpu
0.25	1	3.62e-02	1.13e-01	-9.91e-02	1.93e-02	7.08e-02	2.79e-01	-1.09e-01	8.71e-02	5408 s
0.5	1	3.63e-02	1.12e-01	-9.95e-02	2.03e-02	7.04e-02	2.78e-01	-1.06e-01	9.82e-02	4691 s
1.0	1	3.83e-02	1.10e-01	-1.01e-01	2.32e-02	6.54e-02	2.56e-01	-1.03e-01	1.30e-01	2090 s
2.0	1	3.91e-02	1.08e-01	-1.03e-01	2.75e-02	6.29e-02	2.45e-01	-1.03e-01	1.59e-01	2027 s
0.25	2	3.63e-02	1.13e-01	-9.88e-02	1.82e-02	7.12e-02	2.80e-01	-1.08e-01	7.13e-02	6612 s
0.5	2	3.64e-02	1.13e-01	-9.90e-02	1.85e-02	7.12e-02	2.82e-01	-1.04e-01	7.18e-02	2653 s
1.0	2	3.80e-02	1.11e-01	-9.94e-02	1.93e-02	6.71e-02	2.60e-01	-9.74e-02	7.71e-02	2287 s
2.0	2	3.84e-02	1.12e-01	-1.00e-01	2.12e-02	6.71e-02	2.63e-01	-8.49e-02	9.28e-02	2300 s
(Xiao et al. 2014)		2.06e-02	7.54e-02	-4.76e-02	-0.99e-02	4.94e-02	21.5e-02	-4.07e-02	0.32e-02	

### 3.3 Task 3 - Impact of aortic aneurysm endografts on systemic haemodynamics

The impact of the thoracic stent on mean pressure and pulse pressure of brachiocephalic artery, thoracic aorta, superior mesenteric artery and right iliac artery is reported in [Table 10](#). The change on PWV is also reported. Note that the percentage represents the change from the *reference* case.

[Figure 7](#), [Figure 8](#), [Figure 9](#) and [Figure 10](#) show the impact of the thoracic aortic stent on pressure curves. As before, the time has been normalized to one.

In [\(Hinnen et al. 2007\)](#) it is reported that in a type II endoleak the pressure in the aneurysmal sac is similar to the systemic pressure, at least in the early period of the endoleak. In [\(Schurink et al. 1998\)](#) it is said that the pressure in the aneurysmal sac tends to increase until it reaches the level of diastolic pressure. To simulate an endoleak following the scientific literature, the external pressure of the stented vessel is increased, thus imposing a constant pressure of 70 mmHg, 100 mmHg and 150 mmHg. In this way, the pressure inside the aneurysmal sac pressing on the vessel is simulated.

**Table 10:** Percentage change in hemodynamic parameters compared with the reference case as wave velocity changes in the thoracic aorta: pulse wave velocity (PWV), mean arterial pressure (MAP), pulse pressure (PP).

Wave speed	Brachioc. artery		Thoracic aorta		S. mes. artery		R. iliac artery		
	PWV	MAP	PP	MAP	PP	MAP	PP	MAP	PP
+10%	+3.9%	± 0%	± 0%	± 0%	+2.3%	± 0%	+2.6%	± 0%	+4.3%
+25%	+8.5%	± 0%	+4.7%	± 0%	+2.4%	± 0%	+2.2%	± 0%	+0.8%
+35%	+11.5%	± 0%	+7.1%	± 0%	+4.8%	± 0%	+4.7%	± 0%	+3.3%

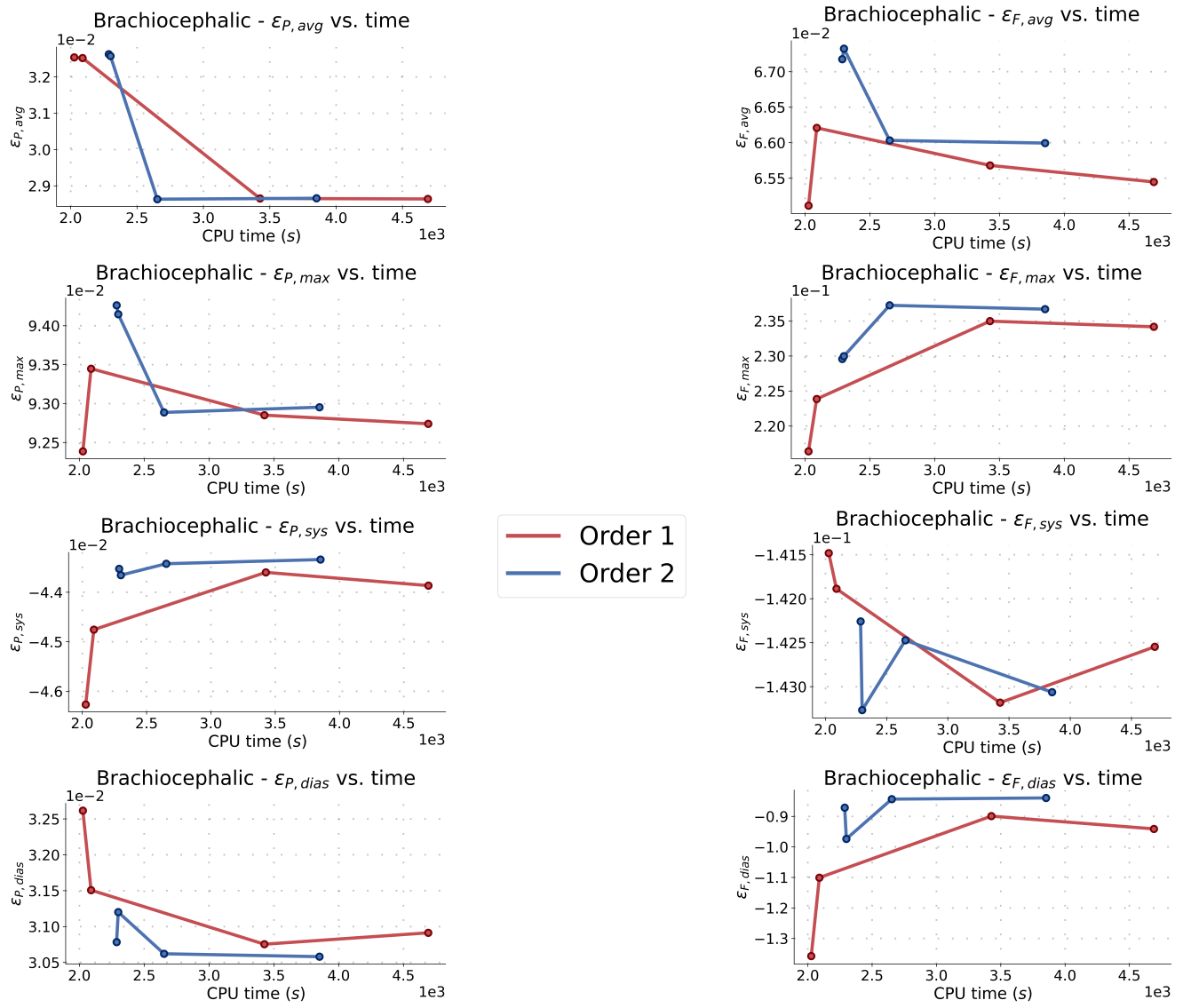


Figure 6: Efficiency plot for the errors reported in Table 7 for the brachiocephalic artery.

The impact of an endoleak in the thoracic stent on mean pressure and pulse pressure of brachiocephalic artery, thoracic aorta, superior mesenteric artery and right iliac artery is reported in Table 11. The change on PWV is also reported. Note that the percentage represents the change from the *reference* case.

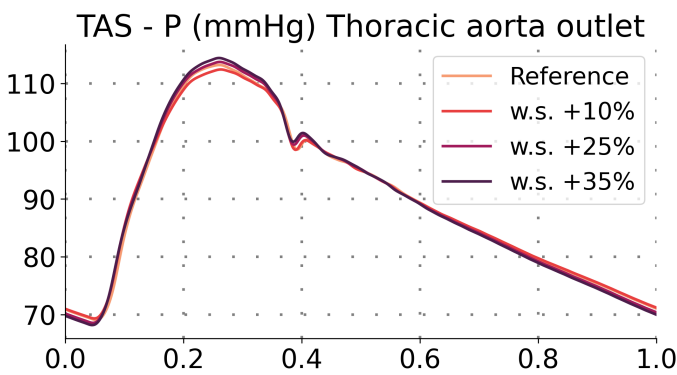
Table 12 shows the change in sectional area in the systole as wave speed and external pressure change. The area considered is at the outlet of the vessel.

Table 11: Percentage change in hemodynamic parameters compared with the reference case as wave velocity and external pressure change in the thoracic aorta: pulse wave velocity (PWV), mean arterial pressure (MAP), pulse pressure (PP).

Wave speed	External pressure	PWV	Brachioc. artery		Thoracic aorta		S. mes. artery		R. iliac artery	
			MAP	PP	MAP	PP	MAP	PP	MAP	PP
+10%	70 mmHg	+0.8%	±0%	+0.9%	±0%	+1.1%	±0%	+1.2%	±0%	+1.3%
	100 mmHg	+0.4%	±0%	+1.0%	+0.1%	+3.3%	±0%	+3.6%	±0%	+4.3%
	150 mmHg	+2.9%	±0%	±0%	+0.2%	+7.8%	±0%	+8.9%	±0%	+9.9%
+25%	70 mmHg	+6.6%	±0%	+4.8%	±0%	+5.0%	±0%	+5.1%	±0%	+5.0%
	100 mmHg	+5.2%	±0%	+4.7%	±0%	+6.5%	±0%	+6.9%	±0%	+7.1%
	150 mmHg	+3.3%	+0.1%	+4.9%	+0.1%	+9.5%	±0%	+10.6%	±0%	+11.1%
+35%	70 mmHg	+9.5%	±0%	+6.9%	±0%	+7.0%	±0%	+7.1%	±0%	+6.9%
	100 mmHg	+8.5%	±0%	+6.6%	±0%	+8.1%	±0%	+8.5%	±0%	+8.7%
	150 mmHg	+6.5%	+0.1%	+5.9%	+0.1%	+10.4%	±0%	+11.4%	±0%	+12.0%

**Table 12:** Percentage change in cross sectional area at systole at the outlet compared to the reference case, as a change in wave velocity and external pressure in the thoracic aorta.

Wave speed	External pressure	Brachio. artery	Thoracic aorta	S. mes. artery	R. iliac artery
+10%	70 mmHg	±0.0%	-2.1%	+0.1%	+0.1%
	100 mmHg	±0.0%	-11.8%	+0.2%	+0.5%
	150 mmHg	-0.2%	-26.7%	+0.6%	+1.1%
+25%	70 mmHg	+0.2%	-5.1%	+0.3%	+0.4%
	100 mmHg	+0.2%	-12.6%	+0.4%	+0.7%
	150 mmHg	+0.1%	-24.4%	+0.7%	+1.1%
+35%	70 mmHg	+0.4%	-6.7%	+0.4%	+0.6%
	100 mmHg	+0.3%	-13.1%	+0.5%	+0.8%
	150 mmHg	+0.2%	-23.2%	+0.8%	+1.2%



**Figure 7:** Case with the thoracic aortic stent (TAS), comparison of pressure in the thoracic aorta with different increases in wave speed (w.s.).

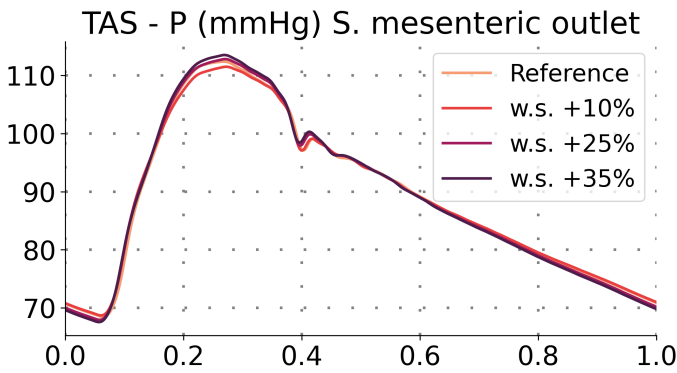


**Figure 9:** Case with the thoracic aortic stent (TAS), comparison of pressure in the superior mesenteric artery with different increases in wave speed (w.s.).

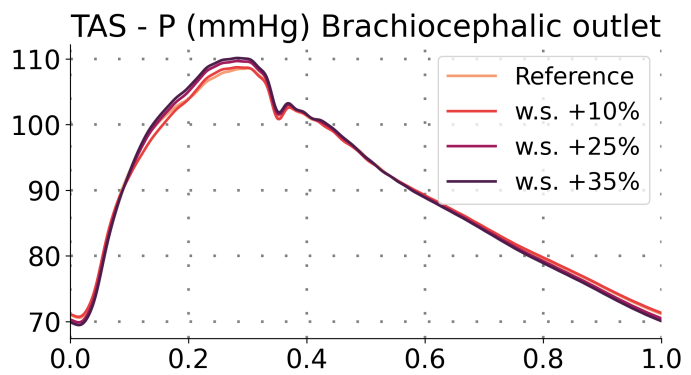


**Figure 8:** Case with the thoracic aortic stent (TAS), comparison of pressure in the brachiocephalic artery with different increases in wave speed (w.s.).

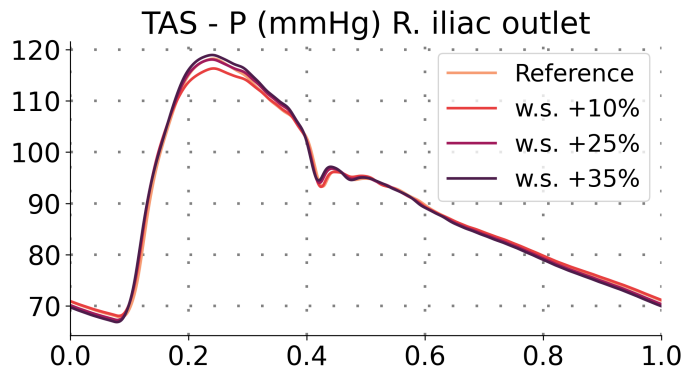


**Figure 10:** Case with the thoracic aortic stent (TAS), comparison of pressure in the right iliac artery with different increases in wave speed (w.s.).

In [Figure 11](#), [Figure 12](#), [Figure 13](#) and [Figure 14](#) is shown the impact of the thoracic aortic stent endoleak on pressure curves. In [Figure 15](#), [Figure 16](#), [Figure 17](#) and [Figure 18](#) is shown the impact of the thoracic aortic stent endoleak on the flow.

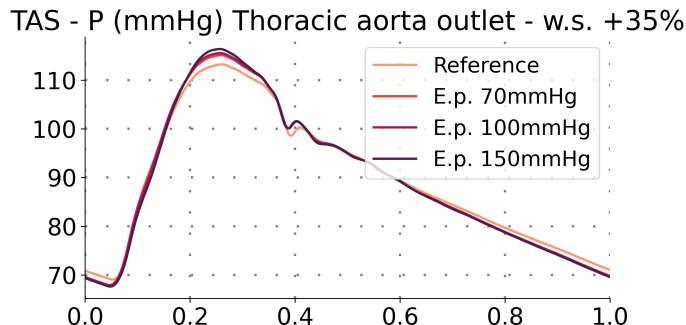


**Figure 11:** Case with the thoracic aortic stent (TAS) (wave speed increase of +35%), comparison of pressure in the thoracic aorta with different external pressure (E.p.).

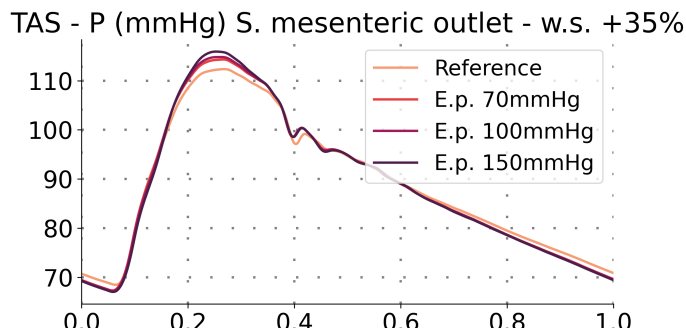


**Figure 13:** Case with the thoracic aortic stent (TAS) (wave speed increase of +35%), comparison of pressure in the superior mesenteric artery with different external pressure (E.p.).

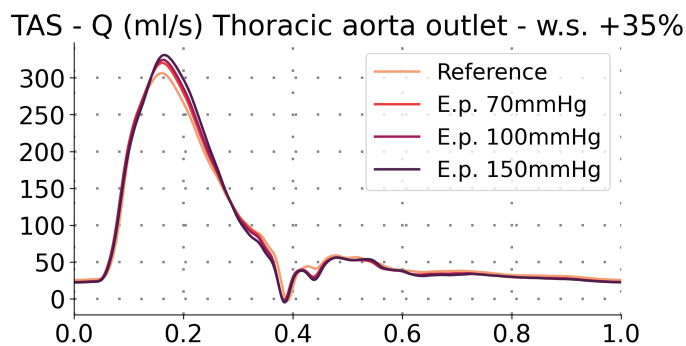


**Figure 15:** Case with the thoracic aortic stent (TAS) (wave speed increase of +35%), comparison of flow in the thoracic aorta with different external pressure (E.p.).

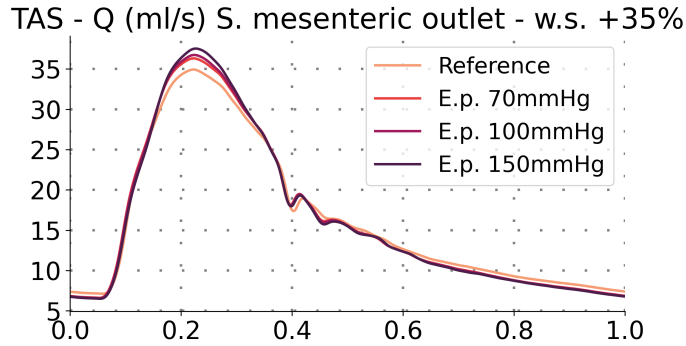


**Figure 17:** Case with the thoracic aortic stent (TAS) (wave speed increase of +35%), comparison of flow in the superior mesenteric outlet with different external pressure (E.p.).

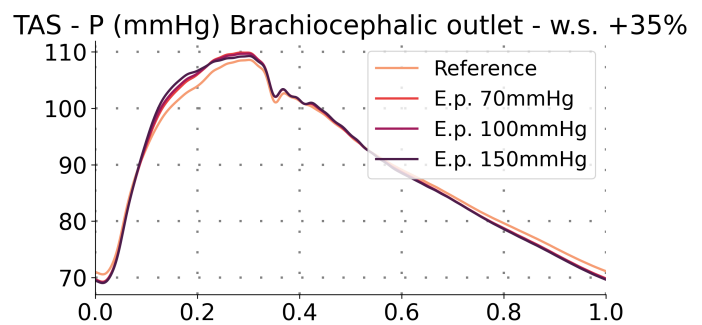


**Figure 12:** Case with the thoracic aortic stent (TAS) (wave speed increase of +35%), comparison of pressure in the brachiocephalic artery with different external pressure (E.p.).

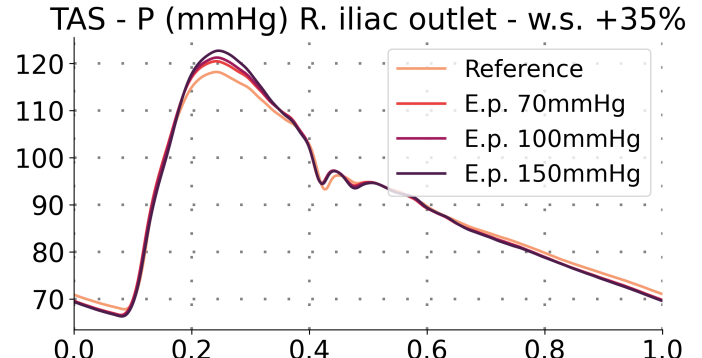


**Figure 14:** Case with the thoracic aortic stent (TAS) (wave speed increase of +35%), comparison of pressure in the right iliac outlet with different external pressure (E.p.).

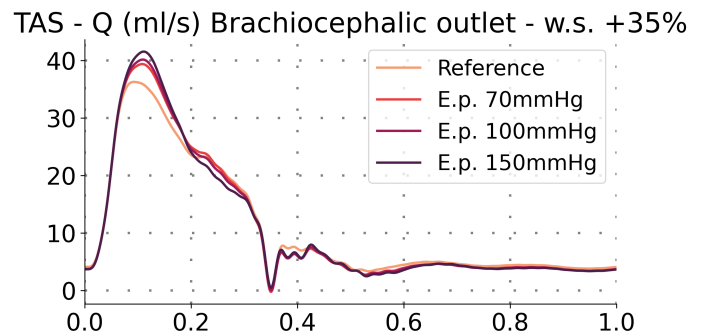


**Figure 16:** Case with the thoracic aortic stent (TAS) (wave speed increase of +35%), comparison of flow in the brachiocephalic artery with different external pressure (E.p.).

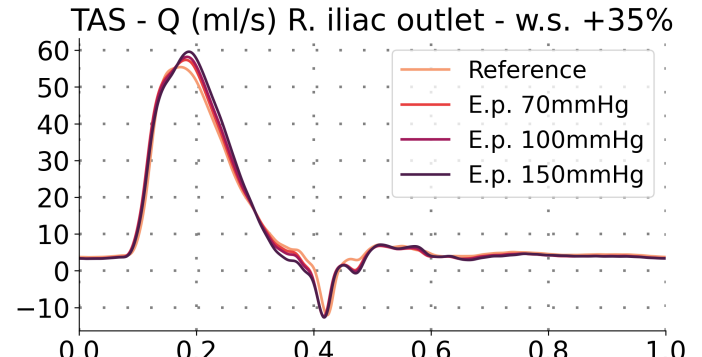


**Figure 18:** Case with the thoracic aortic stent (TAS) (wave speed increase of +35%), comparison of flow in the right iliac artery with different external pressure (E.p.).

## 4 Discussion

### 4.1 Task 1 - Empirical convergence rates

The results of the convergence rate study are reported in [Table 2](#), [Table 3](#), [Table 4](#) and [Table 5](#). In [Figure 3](#) and [Figure 4](#) the exact solution is superimposed on the approximations for different mesh refinements.

Obtained empirical convergence rates are in line with the theory reported in [Section 2.2](#), for both variables  $A$  and  $Q$ . Indeed obtained errors decrease as the mesh becomes finer, ensuring that the numerical solution converges to the exact one with the expected order of accuracy, namely one for the first order method and two for the MH scheme. The CPU time necessary to complete a simulation increases with the growing number of computational cells. Moreover, the MH scheme requires a longer computation time, as expected.

### 4.2 Task 2 - Modelling blood flow in the arterial network used in ([Xiao et al. 2014](#))

[Figure 5](#) reports pressure curves that are qualitatively similar to the 1D curves obtained in ([Xiao et al. 2014](#)). The main deficiency of the curves obtained with the model used is the systolic peak, in both flow and pressure, which is lower than the 1D case of ([Xiao et al. 2014](#)) and much lower than the 3D case. The proximal flow curves are more different from the paper's curves; the distal ones are more similar.

We see that Xiao's 1D model behaves similarly to our own, particularly in how the results align more closely with the 3D model for distal vessels. This observation suggests that the primary cause of the discrepancies observed in the curves can be attributed to the modeling approach: a 1D model lacks the capability to capture as many details as a 3D model can.

We also observe that our model yields results that do not overlap with those from Xiao's 1D model. The use of tapering in the paper, which is not implemented in our model, might be the principal factor contributing to this divergence.

As reported in [Table 6](#), the average values of the pressure and flow curves are very similar to those in the paper.

In [Table 7](#), [Table 8](#) and [Table 9](#) we read the trend of the errors as  $\Delta x$  decreases (see [Section 2.5](#)) and see that the error tends to decrease as the refinement of the mesh increases (i.e., as  $\Delta x$  decreases), concomitant with the increase in CPU time. As inferred from [Figure 5](#), the more proximal cases lead to bigger errors than the distal cases. Overall, however, errors of the same order of magnitude are obtained.

In [Figure 6](#) is shown the trend of errors as a function of execution time for the brachiocephalic artery case. The trends are not regular since they also depend on the other operations performed by the computer during simulation, which may have interfered with the CPU time. From the graphs, it can be seen that the last two simulations ( $\Delta x = 0.5$  and  $\Delta x = 0.25$ ) do not lead to a significant change in error (less than 2%), while they lead to a significant increase in time. For this reason, no further progress was made with mesh refinement. The graphs show that the second-order method performs better in terms of time and error in the case  $\Delta x \leq 0.5$ . For cases  $\Delta x > 0.5$ , the first-order method may be a viable alternative in terms of time, albeit leading to larger errors.

### 4.3 Task 3 - Impact of aortic aneurysm endografts on systemic haemodynamics

#### 4.3.1 Stent case

[Table 10](#) shows the change on pressure indexes due to the change in wave speed.

In ([Mandigers et al. 2023](#)), stents of similar length, placement and oversizing are studied in ex-vivo animal experiments. After the stent implantation, they measured an increase in PWV of +6% and +8%, depending also on the type of stent, thus compatible with our results for the +25% case of wave speed increase. Moreover, they found no significant change in MAP, while there was a significant increase in PP for some stent types (although a percentage average is not reported but only a spaghetti plot). Both results are consistent with what we obtained.

In ([Vardoulis et al. 2011](#)) a 1D model is adapted to simulate a similar thoracic stent in a different manner from what is done in this report. The change in PWV found in the paper is +25%, thus incompatible with our results. The change in PP obtained in the thoracic aorta is +10%, again incompatible with our results. The increase of pressure curves in the paper is much greater than that obtained in this report in [Figure 7](#), [Figure 8](#), [Figure 9](#) and [Figure 10](#).

It should be noted that no images on the variation of flow at varying wave speed were included in the report because no significant differences are obtained.

Among the simulated cases, it is noted that the "wave speed +10%" case is in contrast to the results obtained in the mentioned papers. The +25% case is in accord with the results obtained on animals, but is not compatible with what was obtained from simulations based on human aortic measurements. Although the results obtained are qualitatively compatible with the literature, in quantitative terms they are not comparable. It is possible that the variation in wave speed required to obtain realistic results is much greater than what has been studied.

### 4.3.2 Endoleak case

**Table 11** shows the changes in pressure parameters as wave speed and external pressure increase. In the +10% case of wave speed there is not much variation from the case without endoleak: only the PWV in the 70mmHg and 100mmHg case turns out to be very low, and the PP is greatly varied in the 150mmHg case. In the +25% case, PWV is varied less in percentage than the case without endoleak, while PP variations are greater. Finally, the +35% case shows a decrease in PWV and PP variation in the brachiocephalic artery, while an increase in PP in the other arteries. In all cases there is no significant increase in MAP.

In [Figure 11](#), [Figure 12](#), [Figure 13](#), [Figure 14](#), [Figure 15](#), [Figure 16](#), [Figure 17](#), [Figure 18](#) pressure and flow curves as external pressure changes are shown.

The scientific literature does not present papers reporting results on experiments similar to the one performed in this report, so it is difficult to make comparisons.

With type I and II endoleak, systemic pressure increases, as shown in ([Chaudhuri et al. 2004](#)) and ([Xenos et al. 2003](#)). Although it is difficult to quantitatively compare the results between the papers and the report, the pressure increase is found in all simulated endoleak cases.

The complex phenomenon of endoleaks makes it complicated to compare the results obtained on flow and area with physiological data. What is obtained in **Table 12** is a decrease in area in the stented vessel and a slight increase in area in the nonstented arteries. In reality, not all endoleaks lead to a decrease in vessel diameter. In ([Amesur et al. 1999](#)), for example, a decrease in the size of the aneurysmal sac is found, resulting in a decrease in external pressure. This phenomenon, in the context of our model, would have mitigated the reduction in vessel radius.

Another limitation of the model used is that it does not account for the flow entering the aneurysmal sac, which changes the external pressure and flow. In ([Wolters et al. 2010](#)) it is reported that the flow varies over time, thus making the assumption that the pressure outside the aneurysm is constant unrealistic.

## 5 Conclusions

In this project we showed the validity of one-dimensional (1D) blood flow models in understanding cardiovascular physiology and pathology.

The model used is able to approximately replicate the results of ([Xiao et al. 2014](#)), demonstrating that 1D models can effectively approximate the results of more complex three-dimensional (3D) models. This is a significant result, underscoring the potential of 1D models as a computationally efficient alternative for some applications, especially when computational resources are limited.

In the simulation of thoracic endografts and endoleaks, the 1D model provided results that were partially consistent with existing scientific literature. The simulations indicated that the presence of endografts and endoleaks significantly alters systemic haemodynamics, a critical factor in the clinical evaluation of such interventions.

The model's ability to capture these changes underscores its practical applicability in medical research and its potential clinical utility. However, acknowledging the inherent limitations of 1D models is essential. These limitations arise from the necessary simplifications that are made to represent the complex nature of the circulatory system. It is possible that, in the case of our model, more realistic results would be obtained by implementing tapering, as inferred from the results of Xiao's 1D model, and the time dependence of the aortic sac, as suggested by the scientific literature.

However, we can conclude that our model, although it cannot provide results as realistic as a 3-D model, turns out to be a reliable tool for studying physiological situations in which the geometry of the vessel network does not play a key role.

## References

- Amesur, N. et al. (1999). "Embolotherapy of persistent endoleaks after endovascular repair of abdominal aortic aneurysm with the ancore-endovascular technologies endograft system." In: *Journal of vascular and interventional radiology : JVIR* 10 9, pp. 1175–82. doi: [10.1016/S1051-0443\(99\)70217-4](https://doi.org/10.1016/S1051-0443(99)70217-4).
- Bezerra, C. et al. (2018). "TCT-619 Comparison of one-dimensional (1D) and three-dimensional (3D) models for the estimation of coronary fractional flow reserve through cardiovascular imaging". In: *Journal of the American College of Cardiology*. doi: [10.1016/J.JACC.2018.08.1820](https://doi.org/10.1016/J.JACC.2018.08.1820).
- Chaudhuri, A. et al. (Oct. 2004). "Intrasac pressure waveforms after endovascular aneurysm repair (EVAR) are a reliable marker of type I endoleaks, but not type II or combined types: an experimental study". In: *European Journal of Vascular and Endovascular Surgery: The Official Journal of the European Society for Vascular Surgery* 28.4, pp. 373–378. doi: [10.1016/j.ejvs.2004.07.006](https://doi.org/10.1016/j.ejvs.2004.07.006).
- Commons, Wikimedia (2024). *File:Cardiovascular system - Aorta 1 - Smart-Servier.png* — Wikimedia Commons, the free media repository. [Online; accessed 30-aprile-2024].
- Davis, Frank M et al. (Oct. 1, 2014). "Mechanisms of aortic aneurysm formation: translating preclinical studies into clinical therapies". In: *Heart* 100.19, pp. 1498–1505. doi: [10.1136/heartjnl-2014-305648](https://doi.org/10.1136/heartjnl-2014-305648).
- Formaggia, Luca et al. (2009). *Cardiovascular Mathematics: Modeling and Simulation of the Circulatory System*. Vol. 1. Journal Abbreviation: Modeling, Simulation and Applications Publication Title: Modeling, Simulation and Applications. doi: [10.1007/978-88-470-1152-6](https://doi.org/10.1007/978-88-470-1152-6).
- Ghitti, Beatrice et al. (2023). "Construction of hybrid 1D-0D networks for efficient and accurate blood flow simulations". In: *International Journal for Numerical Methods in Fluids* 95.2, pp. 262–312. doi: <https://doi.org/10.1002/fld.5149>.
- Gray, R. et al. (2018). "Patient-Specific Cardiovascular Computational Modeling: Diversity of Personalization and Challenges". In: *Journal of Cardiovascular Translational Research* 11, pp. 80–88. doi: [10.1007/s12265-018-9792-2](https://doi.org/10.1007/s12265-018-9792-2).
- Harten, Amiram et al. (Jan. 1983). "On Upstream Differencing and Godunov-Type Schemes for Hyperbolic Conservation Laws". In: *SIAM Review* 25.1. Publisher: Society for Industrial and Applied Mathematics, pp. 35–61. doi: [10.1137/1025002](https://doi.org/10.1137/1025002).
- Hinnen, J. W. et al. (Oct. 1, 2007). "Aneurysm Sac Pressure after EVAR: The Role of Endoleak". In: *European Journal of Vascular and Endovascular Surgery* 34.4, pp. 432–441. doi: [10.1016/j.ejvs.2007.05.022](https://doi.org/10.1016/j.ejvs.2007.05.022).
- Leer, Bram van (July 1, 1979). "Towards the Ultimate Conservative Difference Scheme V. A Second-order Sequel to Godunov's Method". In: *Journal of Computational Physics* 32, pp. 101–136. doi: [10.1016/0021-9991\(79\)90145-1](https://doi.org/10.1016/0021-9991(79)90145-1).
- Mandigers, Tim J. et al. (2023). "Comparison of Two Generations of Thoracic Aortic Stent Grafts and Their Impact on Aortic Stiffness in an Ex Vivo Porcine Model". In: *EJVES Vascular Forum* 59, pp. 8–14. doi: [10.1016/j.ejvsvf.2023.04.001](https://doi.org/10.1016/j.ejvsvf.2023.04.001).
- Morris, Paul D. et al. (2015). "Computational fluid dynamics modelling in cardiovascular medicine". In: *Heart* 102, pp. 18–28. doi: [10.1136/heartjnl-2015-308044](https://doi.org/10.1136/heartjnl-2015-308044).
- Prehn, J. et al. (2009). "Oversizing of aortic stent grafts for abdominal aneurysm repair: a systematic review of the benefits and risks". In: *European journal of vascular and endovascular surgery : the official journal of the European Society for Vascular Surgery* 38.1, pp. 42–53. doi: [10.1016/j.ejvs.2009.03.025](https://doi.org/10.1016/j.ejvs.2009.03.025).
- Roth, Gregory A. et al. (2020). "Global Burden of Cardiovascular Diseases and Risk Factors, 1990–2019". In: *Journal of the American College of Cardiology* 76, pp. 2982–3021. doi: [10.1016/j.jacc.2020.11.010](https://doi.org/10.1016/j.jacc.2020.11.010).
- Schurink, G.W.H. et al. (Aug. 1998). "Endoleakage after stent-graft treatment of abdominal aneurysm: Implications on pressure and imaging—an in vitro study". In: *Journal of Vascular Surgery* 28.2, pp. 234–241. doi: [10.1016/S0741-5214\(98\)70159-4](https://doi.org/10.1016/S0741-5214(98)70159-4).
- Taylor, Charles A. et al. (2009). "Patient-specific modeling of cardiovascular mechanics". In: *Annual review of biomedical engineering* 11, pp. 109–34. doi: [10.1146/annurev.bioeng.10.061807.160521](https://doi.org/10.1146/annurev.bioeng.10.061807.160521).
- Townsend, N. et al. (2016). "Cardiovascular disease in Europe: epidemiological update 2016". In: *European heart journal* 37.42, pp. 3232–3245. doi: [10.1093/EURHEARTJ/EHW334](https://doi.org/10.1093/EURHEARTJ/EHW334).
- Vardoulis, O. et al. (Nov. 2011). "Impact of Aortic Grafts on Arterial Pressure: A Computational Fluid Dynamics Study". In: *European Journal of Vascular and Endovascular Surgery* 42.5, pp. 704–710. doi: [10.1016/j.ejvs.2011.08.006](https://doi.org/10.1016/j.ejvs.2011.08.006).
- Wolters, B. J. B. M. et al. (2010). "Computational modelling of endoleak after endovascular repair of abdominal aortic aneurysms". In: *International Journal for Numerical Methods in Biomedical Engineering* 26.3. \_eprint: <https://onlinelibrary.wiley.com/doi/pdf/10.1002/cnm.1283>, pp. 322–335. doi: [10.1002/cnm.1283](https://doi.org/10.1002/cnm.1283).
- Xenos, Eleftherios S. et al. (June 2003). "Distribution of sac pressure in an experimental aneurysm model after endovascular repair: the effect of endoleak types I and II". In: *Journal of Endovascular Therapy: An Official Journal of the International Society of Endovascular Specialists* 10.3, pp. 516–523. doi: [10.1177/15266028031000317](https://doi.org/10.1177/15266028031000317).
- Xiao, Nan et al. (2014). "A Systematic Comparison Between 1-D and 3-D Hemodynamics in Compliant Arterial Models". In: *International Journal for Numerical Methods in Biomedical Engineering* 30.2, pp. 204–231. doi: [10.1002/cnm.2598](https://doi.org/10.1002/cnm.2598).
- Xue, Yan et al. (Apr. 2020). "Association Between Extent of Stent-Graft Coverage and Thoracic Aortic Remodeling After Endovascular Repair of Type B Aortic Dissection". In: *Journal of Endovascular Therapy* 27.2, pp. 211–220. doi: [10.1177/1526602820904164](https://doi.org/10.1177/1526602820904164).